

Article

# Numerical Investigations of Heat Transfer and Fluid Flow Characteristics in Microchannels with Bionic Fish-Shaped Ribs

Quanyue Gao, Haibo Zou and Juan Li \*

School of Mechanical and Electrical Engineering, Nanjing Forestry University, Nanjing 210037, China;  
gaoquanyue@163.com (Q.G.); zb7725313@163.com (H.Z.)

\* Correspondence: lijuan87@njfu.edu.cn

**Abstract:** Microchannel cooling technology is an effective method to solve local thermal stacking. In this paper, four innovative microchannels with bionic fish-shaped rib arrangements (CM-O, CM-R, CM-H, and CM-G) are designed by imitating geese and fish clusters. The heat transfer and flow characteristics of the microchannels are simulated numerically at different Reynold's numbers ( $Re = 200 - 1600$ ). The liquid water temperature and flow field in the four innovative microchannels with bionic ribs are analyzed. The results show that the ribs' arrangement has an influence on the thermal performance of microchannels. Compared to the smooth microchannel (CM), the  $N_u$  of the  $N_u$  microchannels with the bionic fish-shaped ribs increases by 33.00–53.26% while the  $f_{ave}$  increases by 28.63–34.93% at  $Re = 1200$ . The vortices around the ribs are clearly observed which improves the temperature gradient. The performance evaluation criterion (PEC) of CM-H is higher than that of the others. This indicates that the rib arrangement of CM-H is superior for heat dissipation application.

**Keywords:** heat transfer; microchannel; bionic ribs arrangement; numerical simulation; thermal boundary layers



**Citation:** Gao, Q.; Zou, H.; Li, J. Numerical Investigations of Heat Transfer and Fluid Flow Characteristics in Microchannels with Bionic Fish-Shaped Ribs. *Processes* **2023**, *11*, 1861. <https://doi.org/10.3390/pr11061861>

Academic Editors: Ying Xu, Lei Shi and Zhengguang He

Received: 18 April 2023

Revised: 3 June 2023

Accepted: 15 June 2023

Published: 20 June 2023



**Copyright:** © 2023 by the authors. Licensee MDPI, Basel, Switzerland. This article is an open access article distributed under the terms and conditions of the Creative Commons Attribution (CC BY) license (<https://creativecommons.org/licenses/by/4.0/>).

## 1. Introduction

The past several decades have witnessed the phenomenon of increasingly scarce freshwater and fossil energy resources. As the complexity of the system components increases, the surge in thermal stacking reduces the efficiency of many traditional cooling methods. Microchannel cooling technology has become popular for reducing energy consumption and improving transformation efficiency during water treatment processes [1]. It has advantages in small volume and high surface area-to-volume contexts. Tuckerman and Pease [2] were the first to propose the microchannel cooling model. It was found that the temperature distribution in the microchannel can be calculated accurately. Structure optimization [3,4] is the most effective way to improve the performance of microchannels.

A new innovation to enhance heat transfer is applying the bionic principle for the structure optimization of microchannels [5,6]. This expands the heat exchange area and mix fluid and separates the boundary layer by adding bionic ribs [7]. Zhu [8] summarized four processing methods and six bionic structures including the fractal-tree-like structure, conical column structure, hybrid wetting structure, scale structure, concave-convex structure, and superhydrophobic micro-nano structure. Their bionic structure proved to be effective in improving the heat transfer and flow performance. Hydrophobic and hydrophilic patterns are widely used to improve microchannel characteristics. From a microscopic point of view, the microchannel performance is improved by changing the surface material of the wall surface. Current research focuses on drag reduction. Rong [9] proposed ASHS (asymmetric super hydrophobic/hydrophilic surfaces) by influencing fish scales. It was observed that ASHS formed a large surface energy barrier for capturing bubbles and achieved anisotropic drag reduction at high speeds (maximum 4.448 m/s). Rahbarshahlan [10] designed a microchannel which was modeled by two kinds of hydrophilic/hydrophobic patterns. The

results indicated that the use of hydrophobic models could reduce the required power fluid pump by up to 69% and increase heat flux by up to 15%. Changing the heat transfer medium is also a common means. Deng [11] investigated the effect of hydrophilic/hydrophobic patterns on a hot surface and a cold surface, separately. When the hot surface had the pattern, the combined effects of hydrophilic and hydrophobic areas caused evaporation rates higher than the common surface. Conversely, the cold surface could not enhance the performance, because the nanostructures hindered the liquid circulation.

Inspired by the natural transfer systems, all kinds of fractal microchannels were designed to improve the characteristics. These were found to have a lower pressure drop and a higher heat transfer efficiency than traditional heat sinks. Liu et al. [12] proposed a split-and-recombine (SAR) micro-mixer with Y-shaped mixing units. The micromixer had a smaller pressure drop and uniformity of fluid due to its three-dimensional Y-shaped structure. The simulation and experimental results showed that the microchannel aspect ratio had a great impact on its characteristics. Wang et al. [13] developed a new bionic fractal microchannel heat sink based on the fractal theory and topological optimization ideas. The results showed that the introduction of the optimization increased the central velocity of the microchannel by 7.14–18.2%. With fractal dimensions of 1.5 and 2, the flow improvement and Nusselt number improvement were significant.

In addition, some approaches such as utilizing various bionic ribs, fins, and other micro-structures are employed to improve heat transfer performance and friction reduction as well. Chen et al. [14] identified an ultrafast fog harvesting and transport mode in *Sarracenia* trichome. A bionic *Sarracenia* trichome (BST) with an on-demand regular hierarchical microchannel was designed. It improved, threefold, the fog harvesting performance compared with a single-scale structure. Li et al. [15] imitated the riblet structures of shark skins to further enhance thermal performance with low entropy generation. The varied geometry of the flow control split passage improved the fluid exchange. Four innovative microchannels guided the main fluid to the wall and enhanced the uniformity. Huang [16] proposed a tree-shaped MHS (TMHS) with a variable cross-section. Compared with the traditional smooth TMHS, the structure of the variable cross-section further enhanced the heat transfer performance of the TMHS. The results indicated that the TMHS with ribs (TMHS-R) exhibited the highest heat transfer and flow performance. Prasenjit [17] conducted a numerical simulation to study the fluid flow and heat transfer characteristics of novel fish scale bio-inspired structures in microchannels. A fish scale inclination height of 0.026 improved the heat transfer and flow performance as compared to the plain microchannel. Further increments in the inclination height increased the heat transfer rate and the friction factor. Wang [18] proposed a bionic microchannel (BRM) which was based on the wall roughness of the dragonfly wing structure. They investigated the bionic structure introduced by high a speed vortex flow in microchannels and found that this can effectively improve the heat transfer and flow characteristics.

Cluster is a common phenomenon in nature. In order to improve the survival rate and the survival efficiency of the population, fish and birds form a certain interval arrangement through clustering. Ole [19] found that fish swim collectively in certain arrangements during chasing, risk avoidance, and migration to achieve the most desirable results. Fish swim in arrangements (at certain intervals in the same direction) to achieve efficiency and energy saving. Clustering serves different purposes by changing the position of the fish within the swarm as they avoid natural enemies and pursue prey. Inspired by studies of schooling fish, Chung [20] investigated the hydrodynamic performance of a two-dimensional undulating-foil triad in viscous flows via numerical simulation. It was demonstrated that the vortex pair shedding from the leading foil interacting with the boundary-layer of the trailing foil explained the efficiency enhancement. Verma [21] investigated the swimming structure of fish using experimentation and numerical simulation. Fish increase their efficiency by placing themselves off-center, relative to the axis of the leader, and deforming their bodies to synchronize with the momentum of the oncoming vortex. Portugal [22] studied the

mutual position of individuals in a 'V' formation and the effect of the wing-flapping motion on individual energy consumption. It was verified that 'V' formation can save energy.

From the above, it can be seen that achieving high efficiency and low consumption in water treatment processes by using microchannels with a bionic rib arrangement is worth exploring. In this paper, four innovative microchannels with bionic fish-shaped rib arrangements imitating geese and fish clusters are designed. The effect of different rib arrangements on the heat transfer and flow characteristics is investigated. The  $Nu_{ave}$ ,  $f_{ave}$ , and performance evaluation criterion (PEC) are analyzed.

## 2. Physical Model

Based on the simplified structure of fish [23], a kind of rib imitating fish is proposed in this paper, as shown in Figure 1. The fish-shaped rib is designed as a unit where  $a_0 = 0.4$  mm and  $b_0 = 0.2$  mm are the head length and head width, respectively, and  $\alpha_0 = 30^\circ$  is the angle of the tail.



**Figure 1.** Geometric parameters of the fish-shaped ribs.

The ribs are mounted on the bottom wall. As shown in Figure 2, the  $L_{ch} = 78$  mm,  $W_{ch} = 3.2$  mm, and  $H_{ch} = 0.5$  mm are the length, width, and height, respectively. The  $b_w = 0.25$  mm and  $h_w = 0.25$  mm are the sidewall width and base height, respectively.

$$D_h = \frac{4H_{ch}W_{ch}}{2(H_{ch} + W_{ch})} \quad (1)$$

where  $D_h$  is defined as the hydraulic diameter with a value of 0.8648 mm.

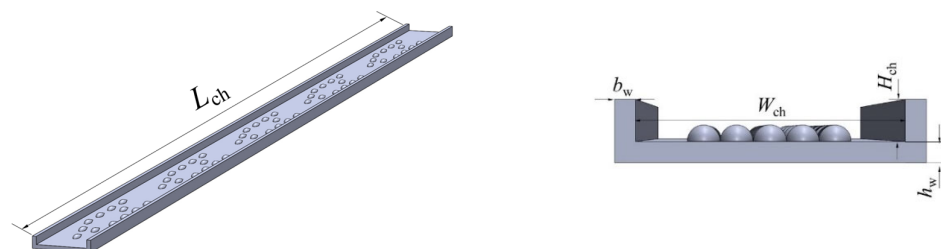


**Figure 2.** Geometric parameters of microchannels.

The model bionic origin of the four microchannels with bionic fish-shaped rib arrangements proposed in this paper is the geese and fish cluster, with the structures shown in Figure 3. CM is defined as a smooth microchannel. CM-O, CM-R, and CM-G imitate three kinds of fish swimming clusters during migrating, chasing, and avoiding. CM-H imitates the flapping of geese in a 'V' shape.  $l_r = 2$  mm,  $l_{c,l} = 0.4$  mm,  $l_{c,s} = 0.2$  mm, and  $l_p = 5$  mm are the spacing between the fish-shaped ribs, the long column spacing, the short column spacing, and spacing between the unit arrangement, respectively, as shown in Figures 4 and 5. In CM-R, there are six periods, and the spacing between unit arrangements is defined as  $l_{p,1}$  with a value of 2.5 mm. The geometric parameters are presented in Table 1.

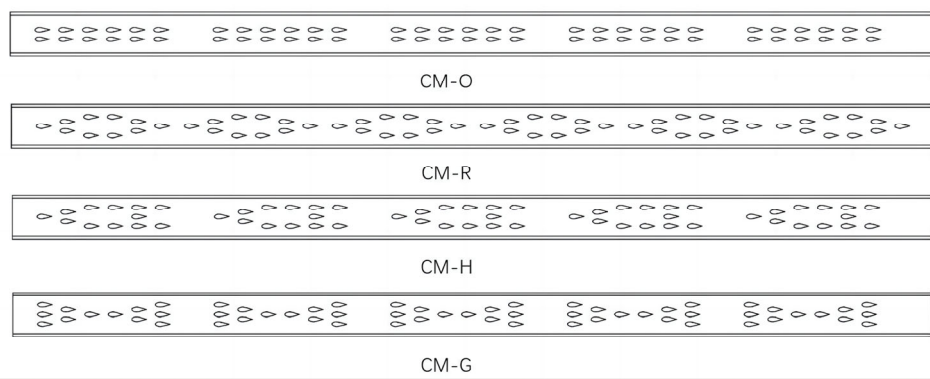


**Figure 3.** Four fish-shaped rib arrangements in the microchannel.

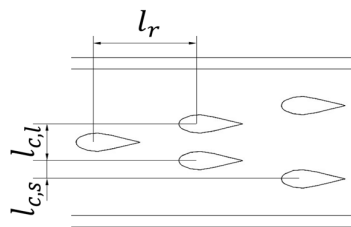


**Figure 4.** The spacing between the fish-shaped ribs.

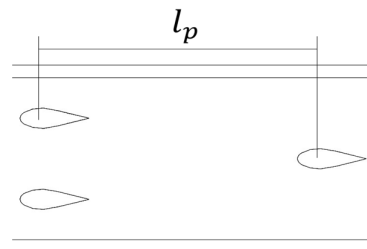


**Figure 5.** The spacing between the unit arrangement.

**Table 1.** Geometric parameters of microchannels and biomimetic ribs.

Variable	Parameter	Variable	Parameter
$a_0$ , mm	0.4	$h_{ch}$ , mm	0.25
$b_0$ , mm	0.2	$D_h$ , mm	0.8648
$\alpha_0$ , °	30	$l_{c,l}$ , mm	0.8
$L_{ch}$ , mm	78	$l_{c,s}$ , mm	0.4
$W_{ch}$ , mm	3.2	$l_r$ , mm	2
$H_{ch}$ , mm	0.5	$l_p$ , mm	5
$b_{ch}$ , mm	0.25	$l_{p,1}$ , mm	2.5

### 3. Mathematical Model

#### 3.1. Boundary Conditions and Numerical Method

The numerical simulation is performed with the computational fluid dynamics (CFD) software *Fluent*. The standard SIMPLE algorithm is employed for the pressure-velocity coupling method. The flow mode is solved by laminar. The microchannel bottom is defined as the boundary of constant heat flux. The heat flux density is  $q_w = 150 \text{ kW/m}^3$ .

The thermophysical properties of fluids and solids are displayed in Table 2. The thermal conductivity  $\lambda_f$  and dynamic viscosity  $\mu_f$  are configured for different physical parameters, as follows, to match the actual circumstances:

$$\lambda_f = -0.51402 + 0.00532T - 3.35719 \times 10^{-6}T^2 - 6.23349 \times 10^{-9}T^3 \quad (2)$$

$$\mu_f = 0.11157 - 9.51523 \times 10^{-4}T + 2.7249 \times 10^{-6}T^2 - 2.61107 \times 10^{-9}T^3 \quad (3)$$

**Table 2.** The thermophysical properties of fluids and solids.

Material	Solid: Aluminum	Fluid: Liquid Water
$C_p$ (J/kg·K)	871	4183
$\rho$ (kg/m <sup>3</sup> )	2700	998.2

The boundary conditions are expressed as follows.

For the inlet, a uniform velocity and constant temperature are adopted:

$$v = v_{in}, v = 0, w = 0, T_f = T_{in} = 298.15K \quad (4)$$

For the outlet: zero pressure.

For the solid–fluid interfaces:

$$\vec{V} = 0, T_f = T_s, \lambda_f \nabla T_f = \lambda_s \nabla T_s \quad (5)$$

For the insulated wall:

$$\lambda_s \nabla T_s = 0 \quad (6)$$

For the inlet velocity, the density of  $v_{in}$  is converted according to the Reynold's number  $Re$ :

$$Re = \frac{\rho_f v_{in} D_h}{\mu_f} \quad (7)$$

where  $\rho$  is the density of the liquid water.

The  $Re$  is set to laminar, ranging from 200 to 1600. Hence, the following assumptions are applied to analyze this model:

- The flow is a Newtonian and incompressible laminar flow.
- The flow is continuous. The N-S equation is still applicable, and there is no slip in the boundary velocity and no jump in temperature.

Based on the above assumptions, the governing equations can be written as follows:  
Continuity equation:

$$\frac{\partial u}{\partial x} + \frac{\partial v}{\partial y} + \frac{\partial w}{\partial z} = 0 \quad (8)$$

Momentum equation:

$$\begin{aligned} \rho_f \left( u \frac{\partial u}{\partial x} + v \frac{\partial u}{\partial y} + w \frac{\partial u}{\partial z} \right) &= -\frac{\partial P}{\partial x} + \mu_f \left( \frac{\partial^2 u}{\partial x^2} + \frac{\partial^2 u}{\partial y^2} + \frac{\partial^2 u}{\partial z^2} \right) \\ \rho_f \left( u \frac{\partial v}{\partial x} + v \frac{\partial v}{\partial y} + w \frac{\partial v}{\partial z} \right) &= -\frac{\partial P}{\partial y} + \mu_f \left( \frac{\partial^2 v}{\partial x^2} + \frac{\partial^2 v}{\partial y^2} + \frac{\partial^2 v}{\partial z^2} \right) \\ \rho_f \left( u \frac{\partial w}{\partial x} + v \frac{\partial w}{\partial y} + w \frac{\partial w}{\partial z} \right) &= -\frac{\partial P}{\partial z} + \mu_f \left( \frac{\partial^2 w}{\partial x^2} + \frac{\partial^2 w}{\partial y^2} + \frac{\partial^2 w}{\partial z^2} \right) \end{aligned} \quad (9)$$

Energy equation (for fluids):

$$u \frac{\partial t}{\partial x} + v \frac{\partial t}{\partial y} + w \frac{\partial t}{\partial z} = \frac{\lambda_f}{\rho_f c_p f} \left( \frac{\partial^2 t}{\partial x^2} + \frac{\partial^2 t}{\partial y^2} + \frac{\partial^2 t}{\partial z^2} \right) \quad (10)$$

Energy equation (for solids):

$$\lambda_s \left( \frac{\partial^2 t}{\partial x^2} + \frac{\partial^2 t}{\partial y^2} + \frac{\partial^2 t}{\partial z^2} \right) = 0 \quad (11)$$

The calculated solutions are considered to be convergent when the normalized residuals of continuity equation, momentum equation, and energy equation are less than  $10^{-4}$ ,  $10^{-4}$ , and  $10^{-6}$ , respectively.

### 3.2. Verification of Independence

In order to appropriately select the mesh size and reduce the convergence time of the simulation within a reasonable range, CM is taken as an example to verify the grid independence. The mesh number is varied as Mesh I (1,500,000), Mesh II (2,000,000), Mesh III (2,500,000), Mesh IV (3,000,000), Mesh V (3,500,000), and Mesh VI (4,000,000), respectively. As a test of the calculated results, Table 3 compares the error rate of  $f_{ave}$  and the error rate of  $N_{u,ave}$ .

**Table 3.** Grid independence examination.

	Mesh Number	$f_{ave}$	Error Rate (%)	$N_{u,ave}$	Error Rate (%)
Mesh I	1,500,000	0.2074	4.40%	9.9078	13.10%
Mesh II	2,000,000	0.2038	2.58%	9.7053	10.79%
Mesh III	2,500,000	0.2002	0.76%	9.0776	3.62%
Mesh IV	3,000,000	0.1999	0.65%	8.9712	2.41%
Mesh V	3,500,000	0.1996	0.49%	8.8489	1.00%
Mesh VI	4,000,000	0.1987	-	8.7602	-

As shown in the Table 3, the deviations of  $f_{ave}$  and  $N_{u,ave}$  of Mesh V are less than 1% at  $Re = 400$ . Therefore, considering the accuracy and calculation cost, Mesh V is considered sufficiently accurate for the calculation. An illustration of the computational meshes of microchannels with bionic rib arrangements is shown in Figure 6.

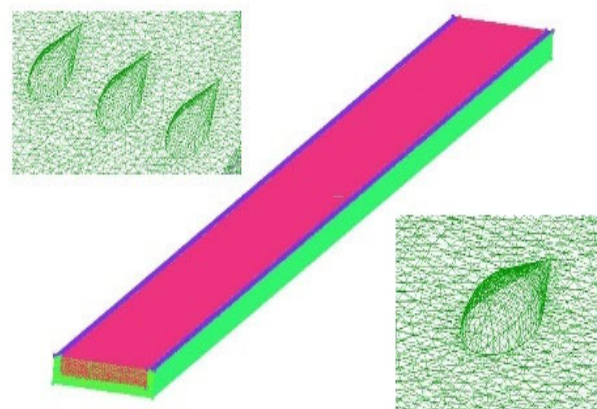


**Figure 6.** Illustration of computational meshes of microchannels with bionic ribs.

In addition, after comparison, the same mesh size is used in other working conditions. Therefore, the element's size of solid domains is chosen as 0.135 and that of fluid domains is chosen as 0.09. In order to increase the accuracy of the fish-shaped ribs' area, the surface and curve meshes are increased to 0.045.

## 4. Data Reduction

The heat and flow characteristics of microchannels can be characterized by the Nusselt number  $Nu$  and average friction coefficient  $f_{ave}$ , respectively. The formulas are as follows.

The  $T_{w,ave}$  is defined as the average temperature of the bottom and wall in microchannels.

The average Nusselt number, which is used to evaluate the heat transfer characteristics, is defined as  $Nu_{ave}$ :

$$Nu_{ave} = \frac{h_{ave} D_h}{\lambda_f} \quad (12)$$

The average friction coefficient is used to evaluate the flow characteristics, as adopted from the Shah studies [24], which is defined as  $f_{ave}$ :

$$f_{ave} = \frac{2\Delta p_{eff} D_h}{\rho_f L_{ch} v^2} \quad (13)$$

where  $\Delta p_{eff}$  is the pressure drop in the microchannel segment, Pa.

The performance evaluation criterion (*PEC*) is introduced to examine the comprehensive thermal and hydraulic performance, which can be described as the better thermal performance with lower pressure drops. *PEC* is calculated, as in [25], as follows:

$$PEC = \frac{Nu/Nu_0}{(f/f_0)^{1/3}} \quad (14)$$

where  $Nu$  is the average Nusselt number of rib arrangements,  $Nu_0$  is the average Nusselt number of CM,  $f$  is the average friction coefficient of rib arrangements,  $f_0$  is the average friction coefficient of CM.

The pressure drop rate is defined as  $\Delta p_{eff}$ :

$$\Delta p_{eff} = p_{in} - p_{out} \quad (15)$$

where  $p_{in}$  is the inlet pressure and  $p_{out}$  is the outlet pressure.

The Prandtl number is a dimensionless combination number that represents the mutual influence of energy and momentum migration processes in a fluid, indicating the relationship between the temperature boundary layer and flow boundary layer, which is defined as:

$$P_r = \frac{C_p \Delta \mu_f}{\lambda_f} \quad (16)$$

## 5. Model Validation

In order to gauge the accuracy of the simulation results, it is essential to carry out a comparison of the  $f_{ave}$  and  $Nu_{ave}$  with theoretical calculations.

Figure 7a depicts the simulated and theoretically calculated values of the  $f_{ave}$  at different  $Re$ s. The theoretical value of the  $f_{ave}$  can be calculated using Equation (13). The simulation results and the theoretical results are in agreement, with a largest relative error of approximately 1%. This demonstrates the reasonableness and validity of this method.

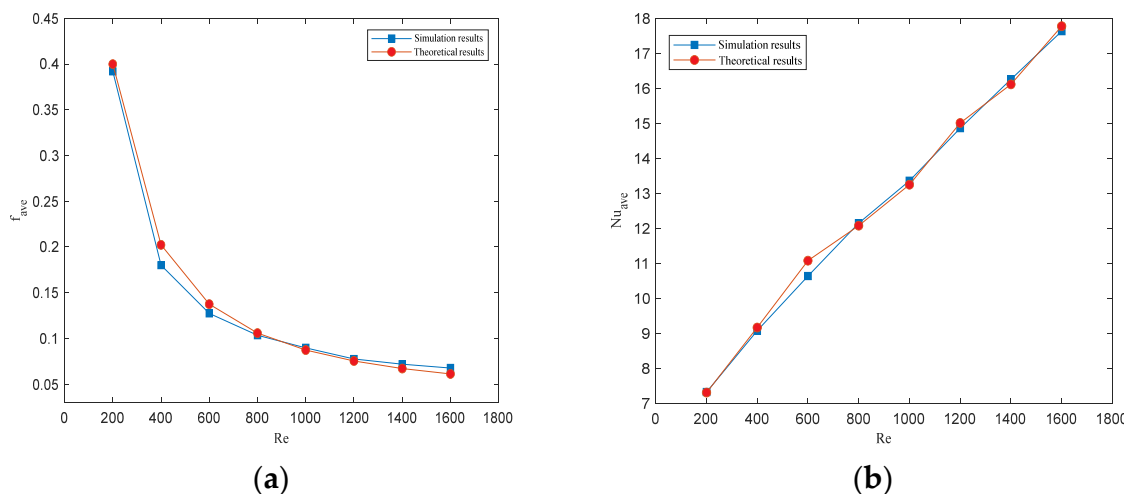


**Figure 7.** Comparison of numerical simulation results with theoretical results. (a) The simulated and theoretically calculated values of  $f_{ave}$ . (b) The simulated and theoretically calculated values of  $Nu_{ave}$ .

Figure 7b depicts the simulated and theoretically calculated values of the  $Nu_{ave}$  at different  $Re$ s. Its theoretical value can be calculated using Equation (18), as in [24].

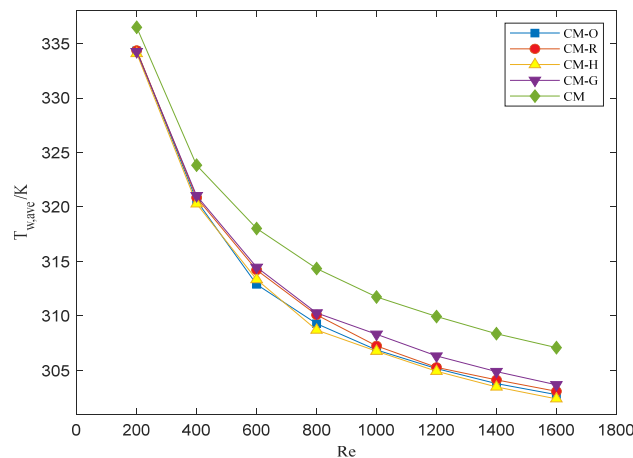
$$Nu_{ave} = \frac{0.3387(Re)^{\frac{1}{2}}(Pr)^{\frac{1}{3}}}{\left[1 + \left(\frac{0.0468}{Pr}\right)^{\frac{2}{3}}\right]^{\frac{1}{4}}} \quad (17)$$

The simulation results and the theoretical results are in agreement, with a largest relative error of approximately 1%. This demonstrates the reasonableness and validity of this method.

## 6. Results and Discussion

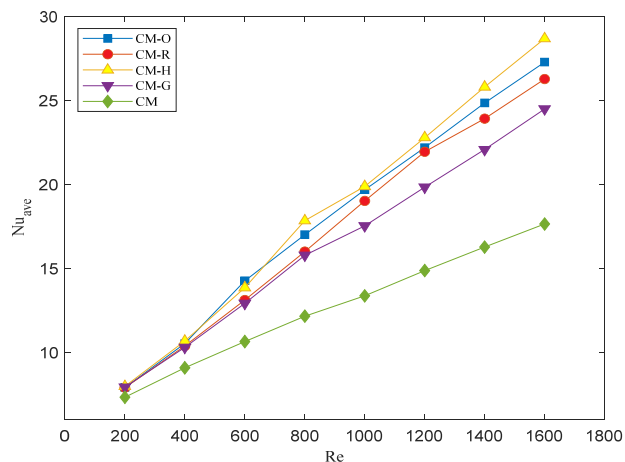
### 6.1. Heat Transfer Characteristics

Under the same heat flux density, a lower temperature of the average wall ( $T_{w,ave}$ ) means that more heat is transferred to the fluid in the microchannels. Heat transfer efficiency is one of the indices to evaluate the heat transfer characteristics of microchannels. As shown in Figure 8, it can be noticed that the  $T_{w,ave}$  of the four microchannels with a bionic rib arrangement is lower than that of CM. The phenomenon proves that the bionic rib arrangement is beneficial to transfer more heat from the wall to the fluid compared with CM. It is evident that as the  $Re$  increases, the  $T_{w,ave}$  of CM and the four innovative microchannels decreases simultaneously, while the gap is more obvious between the  $T_{w,ave}$  of the four proposed microchannels and CM. This means that for a higher inlet velocity, the bionic rib arrangement is more effective.



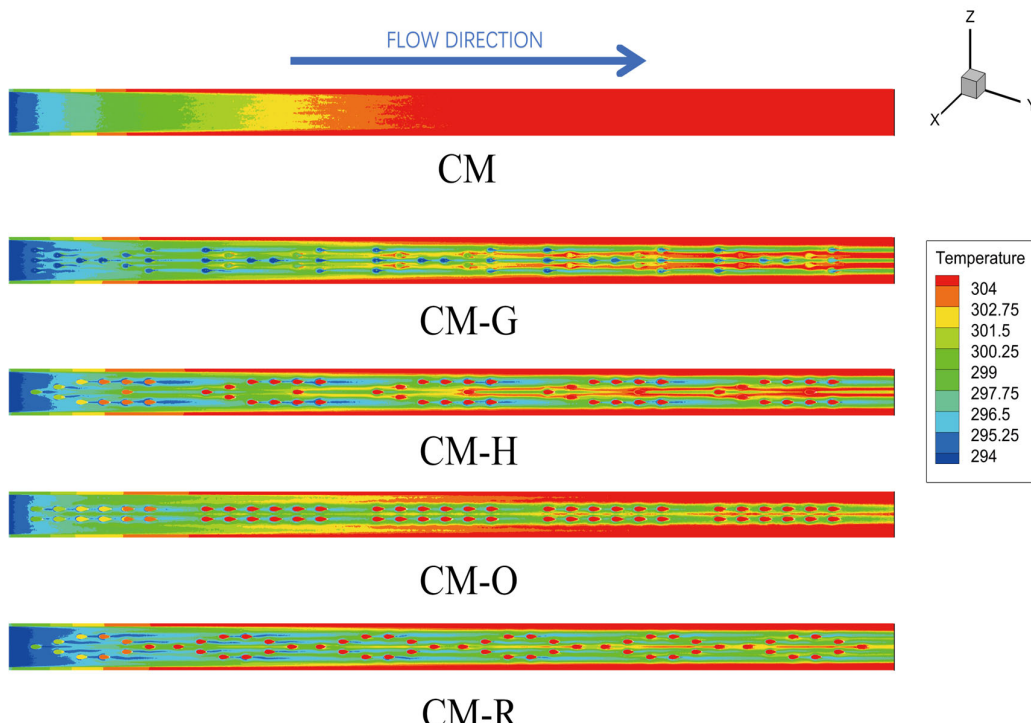
**Figure 8.** Variation of the average wall temperature with Reynold's numbers.

$Nu_{ave}$  is another important indicator of the heat transfer characteristics. Figure 9 shows that the  $Nu_{ave}$  of the four innovative microchannels and CM increases as the  $Re$  increases. In general, the  $Nu_{ave}$  of the four microchannels with bionic rib arrangements is significantly larger than that of CM, which is consistent with the analysis of the average wall temperature. In comparison to CM, the  $Nu_{ave}$  of CM-R and CM-G improves by only 8.24–38.85% and 7.35–35.33% and that of CM-O and CM-H increases by 7.79–48.95% and 8.88–62.59%, which is slightly higher than the other two innovative microchannels. As the  $Re$  increases, the gap of  $Nu_{ave}$  among the different microchannels is also grows. Thus, different bionic rib arrangements and  $Re$ s cause the improvement of heat transfer characteristics in microchannels. As the  $Re$  increases, the velocity gradient of the fluid in the microchannel becomes bigger. The wall temperature and boundary layer thickness for the microchannels with different arrangements demonstrated a larger variation. Hence, the difference in the degree of  $Nu$  is more obvious between the four arrangements as the  $Re$  is rises.



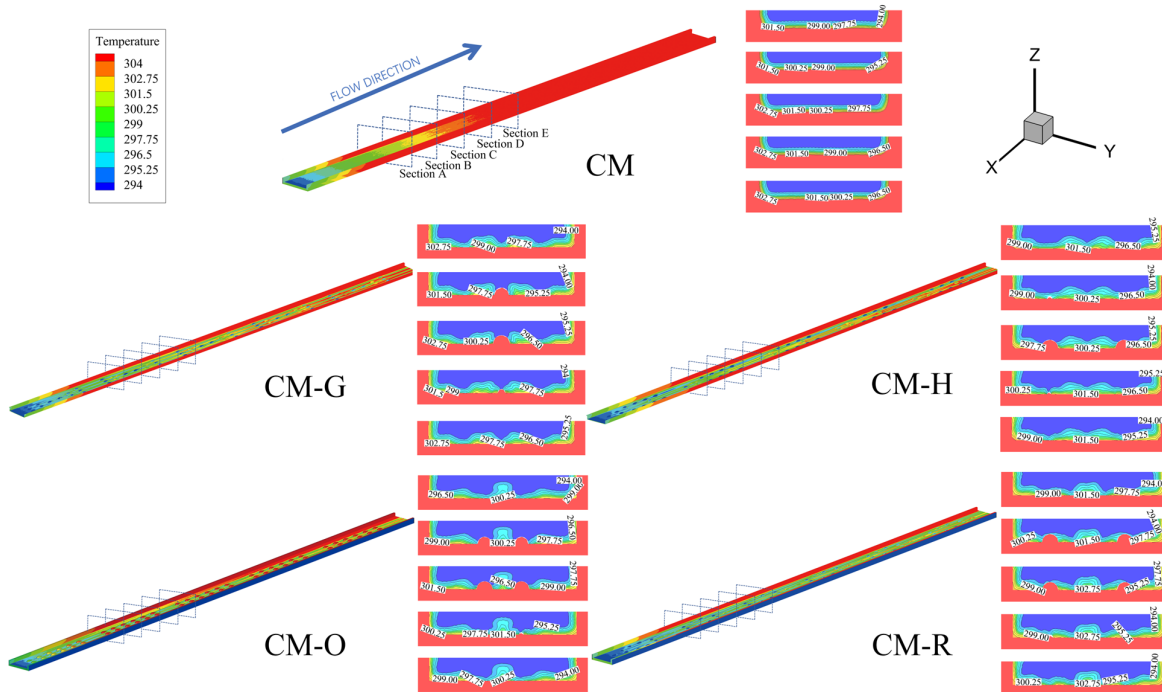
**Figure 9.** Variation of average Nusselt number with Reynold's numbers.

Figure 10 depicts the temperature contours on the x-y horizontal profiles of CM and the four innovative microchannels at  $Re = 1200$ . For the four microchannels with bionic rib arrangements, the increase in the mean fluid temperature is more pronounced when the fluid passes through the rib arrangement. This refers to the fact that the red, hot fluid is concentrated behind the tail of the ribs and in the middle of the microchannel. Compared to CM, the higher temperature fluid in the four proposed microchannels is more distributed, leading to a better heat transfer performance. The region occupied by the red, hot fluid is closer to the entrance profile, indicating that the heat transfer process between the fluid and the wall is faster. A larger region of the redder temperatures in CM-H and CM-O is visible near the walls, where the heat exchange capacity is extremely high. Conversely, the high-temperature fluid of CM-G and CM-R appears further back, indicating that the process of full heat transfer is slower. Hence, it is reasonable to speculate that the form of the rib arrangement directly favors the flow properties of the fluid within the microchannel.



**Figure 10.** The temperature contour on x-y horizontal profile at  $Re = 1200$ .

Figure 11 intuitively reveals the degree of fluid mixing on the  $y$ - $z$  longitudinal profile of the four innovative microchannels and CM at  $Re = 1200$ . Five sections (A, B, C, D, and E) are set as the head, middle, tail of the rib, long space, and shot space in the second rib arrangement. The CM is a smooth wall, and the fluid temperature decreases from the wall to the middle of the microchannels. Due to the viscosity of the fluid, the high-temperature fluid is clustered near the wall without being able to exchange heat effectively with the cold fluid. For the four proposed microchannels, when the high-temperature fluid flows through the rib arrangement, it is squeezed and flows to both sides of the wall. The hot and cold fluids are mixed to enhance the heat transfer efficiency. Moreover, the temperature gradient near the ribs is clearly reduced.



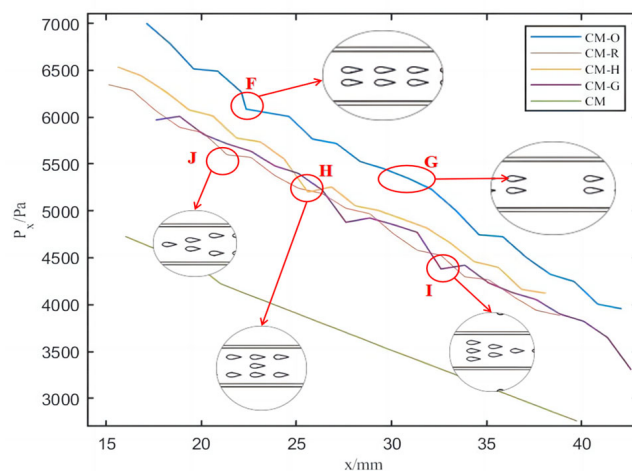
**Figure 11.** The temperature contour on  $y$ - $z$  longitudinal profile at  $Re = 1200$ .

Compared to CM, the CM-O and CM-R have a larger heat transfer area in the center of the microchannels. The ribs of CM-O vertically increase from section A to section E, while those of CM-R vertically decrease after section C. This can be attributed to the larger transverse center distance among the ribs in the CM-O and CM-R, which makes the cold fluid transfer more fully after being squeezed. The heat transfer area of CM-H and CM-G concentrates near the wall and ribs. The temperature gradient of CM-G increases rapidly at the center of the microchannel in section A and section E. This can be attributed to the fact that the cross-sectional area of the microchannel expands rapidly after the fluid flows through the first row of ribs, causing the low-temperature fluid to sink rapidly and increasing the temperature gradient. The CM-H reduces the low and high temperature area which improves the uniformity of the temperature distribution of mainstream fluids. This can be attributed to the fact that the cross-sectional area of CM-H decreases step by step. The movement of the fluid on both sides, after flowing through the ribs, is more fully developed, thus further increasing the heat transfer area.

## 6.2. Fluid Flow Characteristics

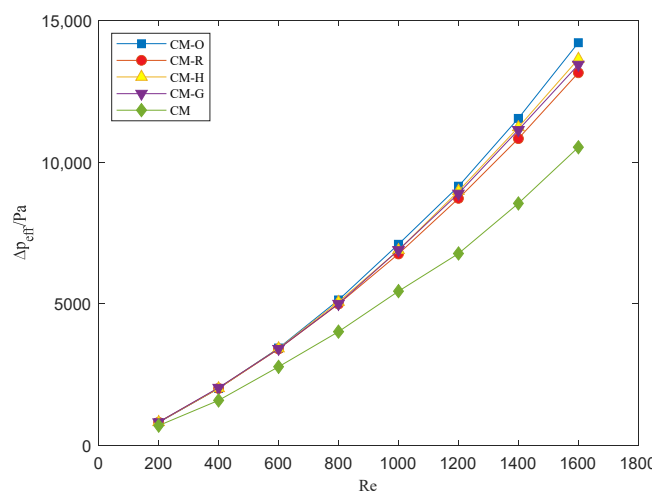
Figure 12 depicts the local pressure along the length in the four innovative microchannels and CM at  $Re = 1200$ . It can be seen that the  $P_x$  decreases periodically along the length. The  $P_x$  of the four microchannels with different rib arrangements is evidently larger than that of CM. Point F, Point H, Point I, and Point J in Figure 10 depict that the ribs result

in a decline and subsequently increase in  $P_x$  at Point G. The pressure drop is related to the cross-sectional area in the microchannel. In terms of the number of ribs, an increase in the number of ribs represents a decrease in the cross-sectional area, which presents a greater degree of decline in  $P_x$  at Point H and Point I. In comparison, Point J and Point F have fewer ribs and smaller pressure drops. This can be attributed to the fact that the cross-sectional area alters along the length due to the bionic rib arrangement, resulting in the pressure drop to vary periodically.



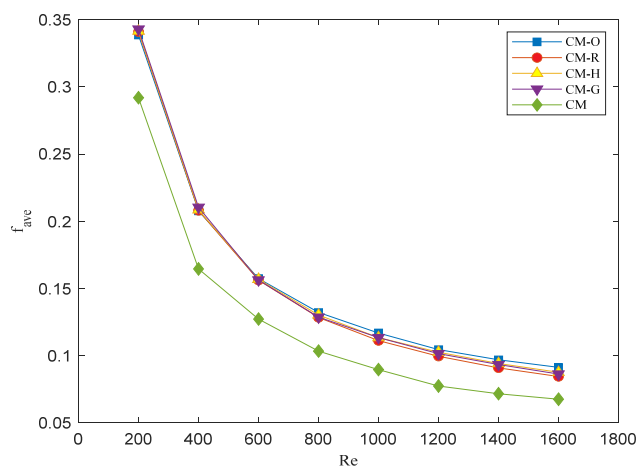
**Figure 12.** Local pressure along the length at  $Re = 1200$ .

Figure 13 shows the pressure drop in the microchannel in relation to the  $Re$ . As shown by the figure, the rib arrangement of CM-O results in a great higher pressure drop than the other microchannels, and the rate of improvement increases with the increasing  $Re$ . At the same time, CM-O has the highest pressure drop, with an increase of almost 50% compared to CM, which slows down the flow velocity.



**Figure 13.** Variation of the pressure drop with Reynold's numbers.

The variations of  $f_{ave}$  at different  $Re$ s are shown in Figure 14. It can be seen that the  $f_{ave}$  of the four microchannels with different rib arrangements is evidently larger than that of CM, and it decreases as the  $Re$  increases. Compared with CM, the  $f_{ave}$  of CM-O, CM-R, CM-H, and CM-G increases by 15.97–35.03%, 16.81–24.96%, 16.98–29.57%, and 17.49–27.68%, respectively. The  $f_{ave}$  of the four microchannels with different rib arrangements is similar. That of CM-O is higher than that of the others, while it cannot control the friction of CM-H.



**Figure 14.** Variation of average friction coefficient with Reynold's numbers.

The x-velocity contour and streamline distribution of the second and third arrangements on the x-y horizontal profile is depicted as Figure 15. It can be noticed that a more pronounced deceleration occurs in the four innovative microchannels. The introduction of the rib arrangements causes the velocity curve in the microchannel to squeeze in all directions. Following the ribs, a greater velocity variation is noticeable, with higher flow velocities close to the ribs and slower flow velocities in the remaining areas. Particularly for CM-O and CM-G, the streamline in the middle of the microchannel is more evidently impacted. In contrast, the outward extrusion of the overall flow in the CM-H and CM-R results in the outer boundary layer fluid being effectively destroyed, which further stagnates the overall velocity.

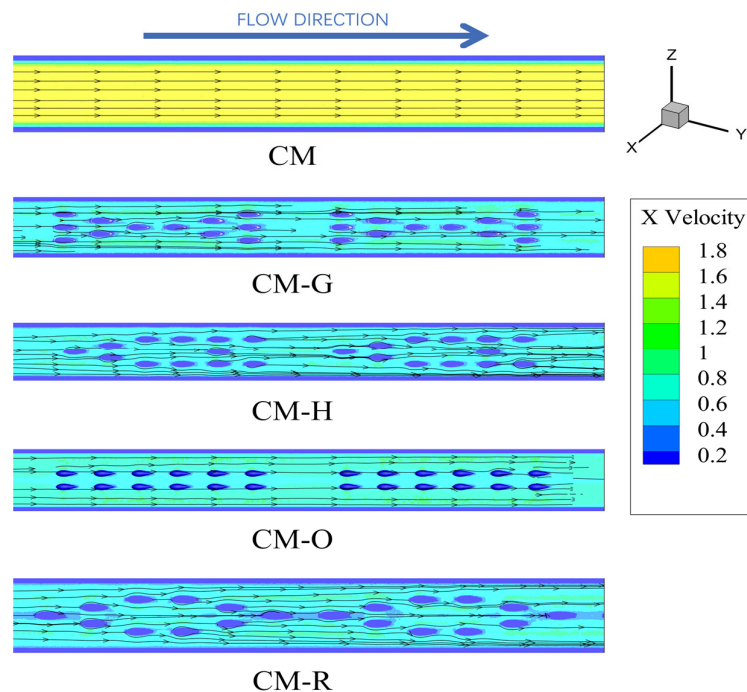


**Figure 15.** The y-velocity contour and streamline distribution of the second and third arrangement on the x-y horizontal profile at  $Re = 1200$ .

Figure 16 illustrates the velocity and streamline distributions of the second and third arrangements on the y-z longitudinal profile at  $Re = 1200$ . Figure 16 shows, vividly, the presence of the distinct vortices after flowing through the rib arrangements in the four innovative microchannels. Due to the sudden increase of the cross-profile passing the

ribs, the fluid lacks the momentum to overcome the combined effect of the flow pressure gradient and the viscous force, and vortices result. It can be observed that vortices cause violent fluid collisions, which make them multi-directional and generate huge fluid mixing, enhancing the heat transfer and friction. This process sufficiently mixes the hot and cold fluids and separates the boundary layers. Hence, it significantly enhances the energy exchange between the fluid and the wall. In general, the excellent flow separation and convergence are attributed to the bionic ribs and arrangement leading to periodic disruption and redevelopment of the thermal boundary layer. This results in an increase in heat transfer and an increase in friction.

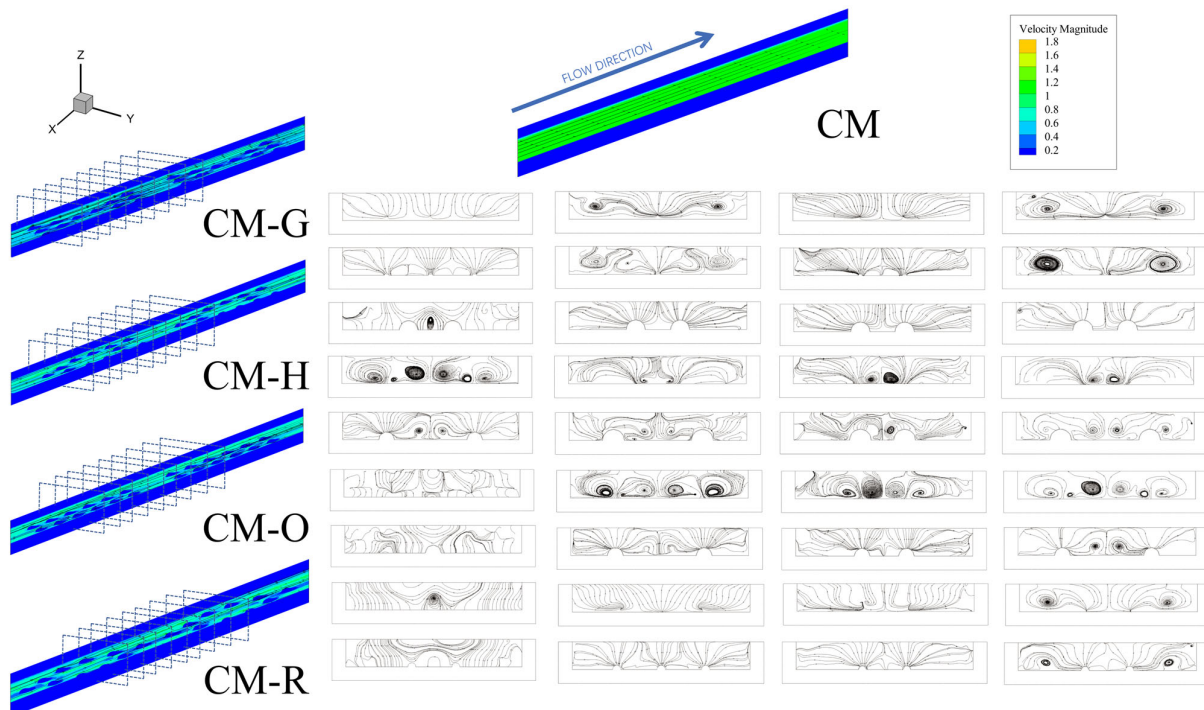


**Figure 16.** The velocity and streamline distributions of the second and third arrangements on the  $y-z$  longitudinal profile at  $Re = 1200$ .

For the streamline distribution of CM-O and CM-G, it can be clearly seen that the flow separation appears from the middle, and a pair of vortices appear after the tail of the bionic ribs from the third profile. In the subsequent flow process, the vortices continue to increase and are interrupted by the walls. Conversely, the vortices of CM-O and CM-G are more pronounced concentrated near the wall. For CM-R, vortices appear both in the middle and wall of the microchannel. They are mostly distributed near the sides of the ribs, scattered and small.

Combined with Figure 11, the CM-O and CM-H vortices are larger than the others. This allows the heat exchange of the fluid in the channel to be more adequate. Compared to CM-O, the vortices of CM-H are closer to the bottom and the wall, implying a better augmentation of the heat transfer by thinning the boundary layer and fluid mixing.

### 6.3. Comprehensive Characteristics Analysis

According to the above results, the heat transfer and flow characteristics of CM-O and CM-H are better than those of the other innovative microchannels. To explore the synthesis of the four microchannels with different rib arrangements, Figure 17 demonstrates the PEC of the four proposed microchannels with respect to  $Re$ . It is found that the PEC of the four microchannels with different rib arrangements all rise with  $Re$  increasing. The variation is 1.03–1.40, 1.02–1.38, 1.03–1.49, and 1.02–1.28, respectively. The efficiency of the microchannels with different rib arrangements increases significantly. The PEC of CM-H

is the largest, being 3.31% greater than CM-O at  $Re = 1200$ . This is due to the fact that the CM-H not only is better at heat transfer but also controls the increasing pressure drop. The sharp increase in the PEC of the four innovative microchannels is inextricably linked to the subsequent transition from laminar to turbulent flow,  $Re = 1200$ . As a corollary, this indicates that CM-H has the best heat transfer characteristic properties with the same power consumption.

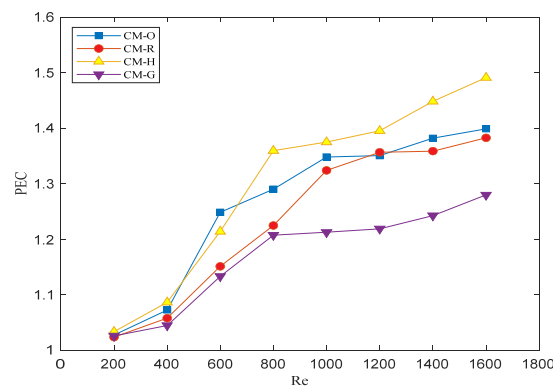


**Figure 17.** Variation of the performance evaluation criterion with Reynold's numbers.

## 7. Conclusions

Based on bionic structure optimization, the flow state of microchannels with bionic fish-shaped rib arrangements is analyzed and optimized in this paper. The effects of the ribs' arrangement on the thermal-hydraulic performance was conducted and the following conclusions are obtained:

1. Compared with CM, the  $T_{w,ave}$  and the  $Nu_{ave}$  of the four microchannels with bionic fish-shaped rib arrangements are clearly increased, while the heat transfer efficiency of CM-H is best. According to the temperature contour analysis, the rib arrangement of CM-H further enhances the mixing of fluids and reduces the wall temperature, which improves the uniformity of the temperature distribution of mainstream fluids.
2. Compared with CM, the local pressure along the length and the  $f_{ave}$  of the four microchannels with bionic fish-shaped rib arrangements are increased while the  $f_{ave}$  of CM-O is larger than that of the others. It can be inferred that the rib arrangement induces periodic interruption and redevelopment of hydraulic and thermal boundary layers, and fluid mixing is intensified by the generated vortices, resulting in the notable convective heat transfer enhancement. The fish-shaped rib arrangement not only increases friction but also enhances heat transfer.
3. Based on the PEC, CM-H is the greatest among the four microchannels with bionic fish-shaped rib arrangements in  $Re$ s ranging from 200–1600. This means that CM-H enhances the transfer characteristics most effectively. Achieving high efficiency and low consumption in water treatment processes by using the bionic rib arrangement CM-H is a worthwhile method.

**Author Contributions:** Conceptualization and review, Q.G. and J.L.; investigation and software, H.Z.; funding acquisition, J.L. All authors have read and agreed to the published version of the manuscript.

**Funding:** This research was funded by National Natural Science Foundation of China grant number 51506098.

**Data Availability Statement:** Not applicable.

**Conflicts of Interest:** The authors declare no conflict of interest.

## Nomenclature

$AR$	Ratio of length to width of microchannel
$Cp_f$	Specific heat of fluid, J/(kg·K)
$Cp_s$	Specific heat of solid, J/(kg·K)
$D_h$	Hydraulic diameter, m
$f_{ave}$	Average friction coefficient
$Nu_{ave}$	Average Nusselt number
$p_{in}$	Inlet pressure, Pa
$p_{out}$	Outlet pressure, Pa
$PEC$	Performance evaluation criterion
$P_r$	Prandtl number
$P_x$	Pressure distribution along the length, Pa
$\Delta p_{eff}$	Pressure drop in microchannel segment, Pa
$Re$	Reynold's number
$T_{in}$	Temperature of inlet, K
$T_{out}$	Temperature of outlet, K
$T_f$	Temperature of fluid, K
$T_s$	Temperature of solid, K
$T_{w,ave}$	Average wall temperature, K
$u, v, w$	Velocity components, m/s
$v_{in}$	Velocity of inlet, m/s
$v_{out}$	Velocity of outlet, m/s
GREEK SYMBOL	
$\lambda_f$	Thermal conductivity of the fluid, W/(m·K)
$\lambda_s$	Thermal conductivity of the solid, W/(m·K)
$\mu_f$	Dynamic viscosity of the fluid, kg/(m·s)
$\rho_f$	Density of fluid, kg/m <sup>3</sup>
$\rho_s$	Density of solid, kg/m <sup>3</sup>
SUBSCRIPTS	
$ave$	Average
$f$	Fluid
$in$	Inlet
$out$	Outlet
$s$	Solid
$w$	Wall

## References

- Zhao, X.; Ma, C.; Park, D.S.; Soper, S.A.; Murphy, M.C. Air bubble removal: Wettability contrast enabled microfluidic interconnects. *Sens. Actuator B Chem.* **2022**, *361*, 131687. [[CrossRef](#)] [[PubMed](#)]
- Tuckerman, D.B.; Pease, R.F.W. High-performance heat sinking for VLSI. *IEEE Electron Device Lett.* **1981**, *2*, 126–129. [[CrossRef](#)]
- Mansoor, M.M.; Wong, K.C.; Siddique, M. Numerical investigation of fluid flow and heat transfer under high heat flux using rectangular micro-channels. *Int. Commun. Heat Mass Transf.* **2012**, *39*, 291–297. [[CrossRef](#)]
- Fan, F.; Qi, C.; Liu, Q.; Sheikholeslami, M. Effect of twisted turbulator perforated ratio on thermal and hydraulic performance of magnetic nanofluids in a novel thermal exchanger system. *Case Stud. Therm. Eng.* **2020**, *22*, 16. [[CrossRef](#)]
- Bei, G.; Ma, C.; Wang, X.; Sun, J.; Ni, X. On the optimal texture shape with the consideration of surface roughness. *Sci. Rep.* **2022**, *12*, 14878. [[CrossRef](#)]
- Han, Q.; Liu, Y.; Li, Z.; Zhang, Y.; Chen, Y. Investigation of energy accommodation coefficient at gas-solid interface of a hypersonic flying vehicle. *Aerosp. Sci. Technol.* **2022**, *126*, 7. [[CrossRef](#)]
- Dong, G.; Chen, B.; Liu, B.; Hounjet, L.J.; Cao, Y.; Stoyanov, S.R.; Yang, M.; Zhang, B. Advanced oxidation processes in microreactors for water and wastewater treatment: Development, challenges, and opportunities. *Water Res.* **2022**, *211*, 118047. [[CrossRef](#)]
- Zhu, Z.; Li, J.; Peng, H.; Liu, D. Nature-Inspired structures applied in heat transfer enhancement and drag reduction. *Micromachines* **2021**, *12*, 656. [[CrossRef](#)]
- Rong, W.T.; Zhang, H.F.; Mao, Z.G.; Chen, L.; Liu, X.W. Stable drag reduction of anisotropic superhydrophobic/hydrophilic surfaces containing bioinspired micro/nanostructured arrays by laser ablation. *Colloid Surf. A-Physicochem. Eng. Asp.* **2021**, *622*, 126712. [[CrossRef](#)]

10. Rahbarshahlan, S.; Esmaeilzadeh, E.; Khosroshahi, A.R.; Bakhshayesh, A.G. Numerical simulation of fluid flow and heat transfer in microchannels with patterns of hydrophobic/hydrophilic walls. *Eur. Phys. J. Plus.* **2020**, *135*, 22. [[CrossRef](#)]
11. Deng, W.; Wang, T.Q.; Chen, J.T.; He, S.H.; Dong, K.J.; Zhao, J.Y. Performance enhancement of nanoscale heat pipe with hydrophilic/hydrophobic pattern. *Int. Commun. Heat Mass Transf.* **2023**, *144*, 14. [[CrossRef](#)]
12. Liu, G.J.; Wang, M.; Dong, L.T.; Zhu, D.Y.; Wang, C.H.; Jia, Y.H.; Li, X.B. A novel design for split-and-recombine micromixer with double-layer Y-shaped mixing units. *Sens. Actuator A-Phys.* **2022**, *341*, 8. [[CrossRef](#)]
13. Wang, Y.W.; Sun, L.; Qi, C.; Yu, J.; Zhang, W.J. Topology optimization of a novel bionic fractal microchannel applied in thermal management of electronic components. *Asia-Pac. J. Chem. Eng.* **2023**, *18*, e2900. [[CrossRef](#)]
14. Chen, H.W.; Ran, T.; Zhang, K.T.; Chen, D.K.; Gan, Y.; Wang, Z.L.L.; Jiang, L. Highly Efficient Multiscale Fog Collector Inspired by Sarracenia Trichome Hierarchical Structure. *Glob. Chall.* **2021**, *5*, 11. [[CrossRef](#)]
15. Li, P.; Guo, D.Z.; Huang, X.Y. Heat transfer enhancement, entropy generation and temperature uniformity analyses of shark-skin bionic modified microchannel heat sink. *Int. J. Heat Mass Transf.* **2019**, *146*, 10. [[CrossRef](#)]
16. Huang, P.N.; Dong, G.P.; Zhong, X.N.; Pan, M.Q. Numerical investigation of the fluid flow and heat transfer characteristics of tree-shaped microchannel heat sink with variable cross-section. *Chem. Eng. Process.* **2020**, *147*, 107769. [[CrossRef](#)]
17. Prasenjit, D.; Gaurav, H.; Saha, S.K. Experimental and numerical investigations of fluid flow and heat transfer in a bioinspired surface enriched microchannel. *Int. J. Therm. Sci.* **2019**, *135*, 44–60. [[CrossRef](#)]
18. Wang, Z.; Li, B.G.; Luo, Q.Q.; Zhao, W.L. Effect of wall roughness by the bionic structure of dragonfly wing on microfluid flow and heat transfer characteristics. *Int. J. Heat Mass Transf.* **2021**, *173*, 121201. [[CrossRef](#)]
19. Misund, O.A.; Aglen, A.; Frønæs, E. Mapping the shape, size, and density of fish schools by echo integration and a high-resolution sonar. *ICES J. Mar. Sci.* **1995**, *52*, 11–20. [[CrossRef](#)]
20. Chung, M. Hydrodynamic Performance of Two-Dimensional Undulating Foils in Triangular Formation. *J. Mech.* **2011**, *27*, 177–190. [[CrossRef](#)]
21. Verma, S.; Novati, G.; Koumoutsakos, P. Efficient collective swimming by harnessing vortices through deep reinforcement learning. *Proc. Natl. Acad. Sci. USA* **2018**, *115*, 5849–5854. [[CrossRef](#)] [[PubMed](#)]
22. Portugal, S.J.; Hubel, T.Y.; Fritz, J.; Heese, S.; Trobe, D.; Voelkl, B.; Hailes, S.; Wilson, A.M.; Usherwood, J.R. Upwash exploitation and downwash avoidance by flap phasing in ibis formation flight. *Nature* **2014**, *505*, 399–402. [[CrossRef](#)] [[PubMed](#)]
23. Xu, C. Study on the pulsating Flow and Heat Transfer Characteristics of Nanofluids in a Deformed Microfine Array Channel. *China Acad. J.* **2021**, *2*, 166. [[CrossRef](#)]
24. Shah, R.K.; London, A.L. *Laminar Flow Forced Convection in Ducts*; Academic Press: Cambridge, MA, USA, 1978; pp. 366–384. [[CrossRef](#)]
25. Li, P.; Xie, Y.H.; Zhang, D.; Xie, G.N. Heat Transfer Enhancement and Entropy Generation of Nanofluids Laminar Convection in Microchannels with Flow Control Devices. *Entropy* **2016**, *18*, 15. [[CrossRef](#)]

**Disclaimer/Publisher's Note:** The statements, opinions and data contained in all publications are solely those of the individual author(s) and contributor(s) and not of MDPI and/or the editor(s). MDPI and/or the editor(s) disclaim responsibility for any injury to people or property resulting from any ideas, methods, instructions or products referred to in the content.